JGR Solid Earth

RESEARCH ARTICLE
10.1029/2022JB026045

Seismotectonics of the Blanco Transform Fault System, Northeast Pacific: Evidence for an Immature Plate Boundary

Yu Ren[1], **Dietrich Lange**[1], **and Ingo Grevemeyer**[1]

[1]GEOMAR Helmholtz Centre for Ocean Research Kiel, Kiel, Germany

Key Points:

- Local seismicity of the Blanco transform fault system (BTFS) reveals along-strike variations dominated by strike-slip and oblique dip-slip
- The BTFS developed from non-transform offsets rather than discrete transform faults in response to plate rotation and ridge propagation
- The BTFS consists of a mature plate boundary in the east and an immature system in the west, separated by a central spreading center

Supporting Information:

Supporting Information may be found in the online version of this article.

Correspondence to:

Y. Ren,
yren@geomar.de

Citation:

Ren, Y., Lange, D., & Grevemeyer, I. (2023). Seismotectonics of the Blanco transform fault system, northeast Pacific: Evidence for an immature plate boundary. *Journal of Geophysical Research: Solid Earth*, *128*, e2022JB026045. https://doi.org/10.1029/2022JB026045

Received 14 NOV 2022
Accepted 27 FEB 2023

Author Contributions:

Conceptualization: Ingo Grevemeyer
Formal analysis: Yu Ren, Ingo Grevemeyer
Investigation: Yu Ren
Methodology: Dietrich Lange
Resources: Ingo Grevemeyer
Supervision: Dietrich Lange, Ingo Grevemeyer
Visualization: Yu Ren
Writing – original draft: Yu Ren
Writing – review & editing: Dietrich Lange, Ingo Grevemeyer

Abstract At the Blanco transform fault system (BTFS) off Oregon, 138 local earthquakes and 84 double-couple focal mechanisms from ocean-bottom-seismometer recordings jointly discussed with bathymetric features reveal a highly segmented transform system without any prominent fracture zone traces longer than 100 km. In the west, seismicity is focused at deep troughs (i.e., the West and East Blanco, and Surveyor Depressions). In the east, the BTFS lacks a characteristic transform valley and instead developed the Blanco Ridge, which is the most seismically active feature, showing strike-slip and dip-slip faulting. Sandwiched between the two main segments of the BTFS is the Cascadia Depression, representing a short intra-transform spreading segment. Seismic slip vectors reveal that stresses at the eastern BTFS are roughly in line with plate motion. In contrast, stresses to the west are clockwise skewed, indicating ongoing reorganization of the OTF system. As we observed no prominent fracture zones at the BTFS, plate tectonic reconstructions suggest that the BTFS developed from non-transform offsets rather than pre-existing transform faults during a series of ridge propagation events. Our observations suggest that the BTFS can be divided into two oceanic transform systems. The eastern BTFS is suggested to be a mature transform plate boundary since ~0.6 Ma. In contrast, the western BTFS is an immature transform system, which is still evolving to accommodate far-field stress change. The BTFS acts as a natural laboratory to yield processes governing the development of oceanic transform faults.

Plain Language Summary The Blanco transform fault system (BTFS) northwest off the coast of Oregon is seismically very active. We used 1 year of ocean bottom seismometer data collected between September 2012 and October 2013 to locate 138 local earthquakes. The events align perfectly with the morphologic features of the BTFS, dividing the BTFS into five transform segments and two short intra-transform spreading centers. Furthermore, we observe different seismotectonic behaviors of the western and eastern BTFS based on the along-strike variation in morphology, magnetization, focal depth distribution, and strain partitioning. Although many segmented oceanic transform systems were formed from a single transform fault in response to rotations in plate motion, the BTFS turns out to be originated from non-transform offsets between ridge segments, as we observed no prominent fracture zone traces neither in morphology nor gravity field data. A clockwise shift in the Juan de Fuca/Pacific pole of rotation at ~5 Ma followed by a series of ridge propagation events initiated the formation of the BTFS, integrated each segment of the BTFS by shortening the ridge segments in between. Our observations suggest that the Blanco Ridge and the Gorda transform segment in the eastern BTFS were formed at ~1.6 and 0.6 Ma, respectively, and ever since, the eastern BTFS became a mature transform boundary. In contrast, seismic slip vectors comparing to plate motion directions reveal that stresses in the western BTFS are systematically skewed, suggesting the immature transform plate boundary is still adjusting to the new stress regime.

1. Introduction

Oceanic transform faults (OTFs) offset the spreading axis by tens to hundreds of kilometers and hence are some of the most noticeable tectonic features in deep ocean basins. Plate tectonics defined OTFs as first-order tectonic discontinuities of mid-ocean ridges and long-lived tectonic features (Carbotte et al., 2015; Macdonald et al., 1988; J. T. Wilson, 1965). In the Atlantic Ocean, most large OTFs were introduced during rifting; thus, their fracture zones cut through the entire ocean basin (Matthews et al., 2011; J. T. Wilson, 1965). In the Pacific Ocean, some fracture zones represent the longest linear features on our planet, like the over 10,000 km long Clipperton fracture zone (Menard, 1967). However, north of ~41°N, none of the long and prominent fracture zone traces of the Pacific is directly linked to any OTF offsetting the modern spreading ridges in the eastern Pacific (Matthews et al., 2011). The collision of the Farallon spreading center with North America at ~28 Ma caused a major

reorientation of the tectonic plate boundaries (Atwater & Stock, 1998), giving birth to the Juan de Fuca and the Cocos plates and causing a number of abandoned spreading ridges in the eastern Pacific Ocean (Lonsdale, 2005).

In the northeast Pacific, the northward migration of the Mendocino triple junction (Atwater & Stock, 1998) and the Cobb hotspot (Karsten & Delaney, 1989) controlled the recent plate reorganization. Between 20 and 2 Ma, spreading at the Juan de Fuca Ridge (JdFR) and Gorda Ridge (GR) occurred without developing any OTF as the area lacks evidence of any prominent fracture zone longer than 100 km (Matthews et al., 2011). Instead, magnetic anomalies and bathymetric features suggest that the geometry of both ridges was controlled by ridge propagation (Carbotte et al., 2008; Marjanović et al., 2011; D. S. Wilson, 1993; Wilson et al., 1984), probably governed by the Cobb hotspot, which is today located under the JdFR (Karsten & Delaney, 1989). The Blanco transform fault system (BTFS) is located northwest off the coast of Oregon and has a total length of ∼350 km (Figure 1 and Figure S1 in Supporting Information S1). The evolution and formation of the BTFS are inherently related to plate boundary reconfiguration by propagating ridges (Embley & Wilson, 1992).

The formation of the BTFS resulted from a clockwise rotation of plate motion, occurring at ∼5 Ma (D. S. Wilson, 1993; Wilson et al., 1984). Between ∼5 and ∼1.8 Ma, three ridge propagation events set the stage for the main features characterizing the BTFS today. Embley and Wilson (1992) suggested that the propagating rift tip would be linked to the adjacent spreading segment by an OTF. However, this would imply that new OTFs develop continuously and instantaneously during propagation. Instead, it might be more realistic to consider the broad transform zone model (McKenzie, 1986; D. S. Wilson, 1988, 1990) that the propagating ridge extends at a constant rate as it takes over the spreading role from the doomed rift. Propagation is going to leave behind a characteristic V-shaped pseudofault. Such pseudofaults were observed on either side of the JdFR (e.g., Marjanović et al., 2011), at the Mid-Atlantic Ridge (Dannowski et al., 2018; Kahle et al., 2016) or in Iceland (Karson, 2017; Morgan & Kleinrock, 1991). During propagation, the spreading responsibility is transferred from one ridge segment to the other. Active deformation occurs in a broad transform zone as material shears in the process of being transferred from one plate to the other. This results in a sheared zone between the failed ridge and its inner pseudofault instead of creating a simple OTF (McKenzie, 1986). The complex tectonic features of a transform zone can perhaps best be seen in northern Iceland, where propagation generated the Tjörnes transfer zone with deformation in three different strands (Karson, 2017) with the basins of the Grimsey Fault Zone in the north roughly mimicking the depressions of the western BTFS. However, while propagation in Iceland is continuing, it has stopped ∼1.8 Ma at the BTFS (D. S. Wilson, 1993).

Therefore, the BTFS represents a natural laboratory to study the development of an OTF system after ridge propagation and shortening of spreading segments terminated. Karson (2017) noted that ridge parallel strike-slip faults in south Iceland transform zone are reactivated spreading related normal faults. It might be reasonable to hypothesize that features formed within the shear zone between the propagating ridge and the doomed ridge favored the nucleation of new strike-slip segments of an immature OTF.

Here, we study the seismotectonic of the BTFS using constraints from 1 year of ocean-bottom-seismometer (OBS) data obtained in 2013 (Figure S2 in Supporting Information S1) during the Blanco Transform OBS Experiment (Kuna, 2020; Nábělek & Braunmiller, 2012). Local seismicity and focal mechanisms along the entire BTFS reveal recent faulting and deformation. Bathymetry (Ryan et al., 2009) and aeromagnetic (Bankey et al., 2002) data sets are also used to corroborate our seismicity study findings. We further discuss results in terms of stresses acting at a mature fault system or a still evolving OTF.

2. Tectonic Setting

The BTFS represents a major left-lateral ridge-crest discontinuity and connects the intermediate-spreading GR in the southeast with the JdFR in the northwest (Figure 1a). The BTFS is a highly segmented OTF system marked by topographic highs (the Parks Plateau [PP] and the Blanco Ridge [BR]) and deep troughs (the West and East Blanco Depressions [WBD and EBD], Surveyor Depression [SUR], Cascadia Depression [CAS], and Gorda Depression [GD]) (Dauteuil, 1995; Embley & Wilson, 1992), as well as the Cascadia Channel cutting into the intersection between the CAS and the BR. An interesting feature is that the plate boundary along the BTFS is characterized by a positive magnetic anomaly (Figure 1b).

Teleseismic analysis (e.g., Dziak et al., 1991) inferred the seismic coupling strength is different along the west and east segments of BTFS, although the routine event locations along the BTFS are scattered and systematically

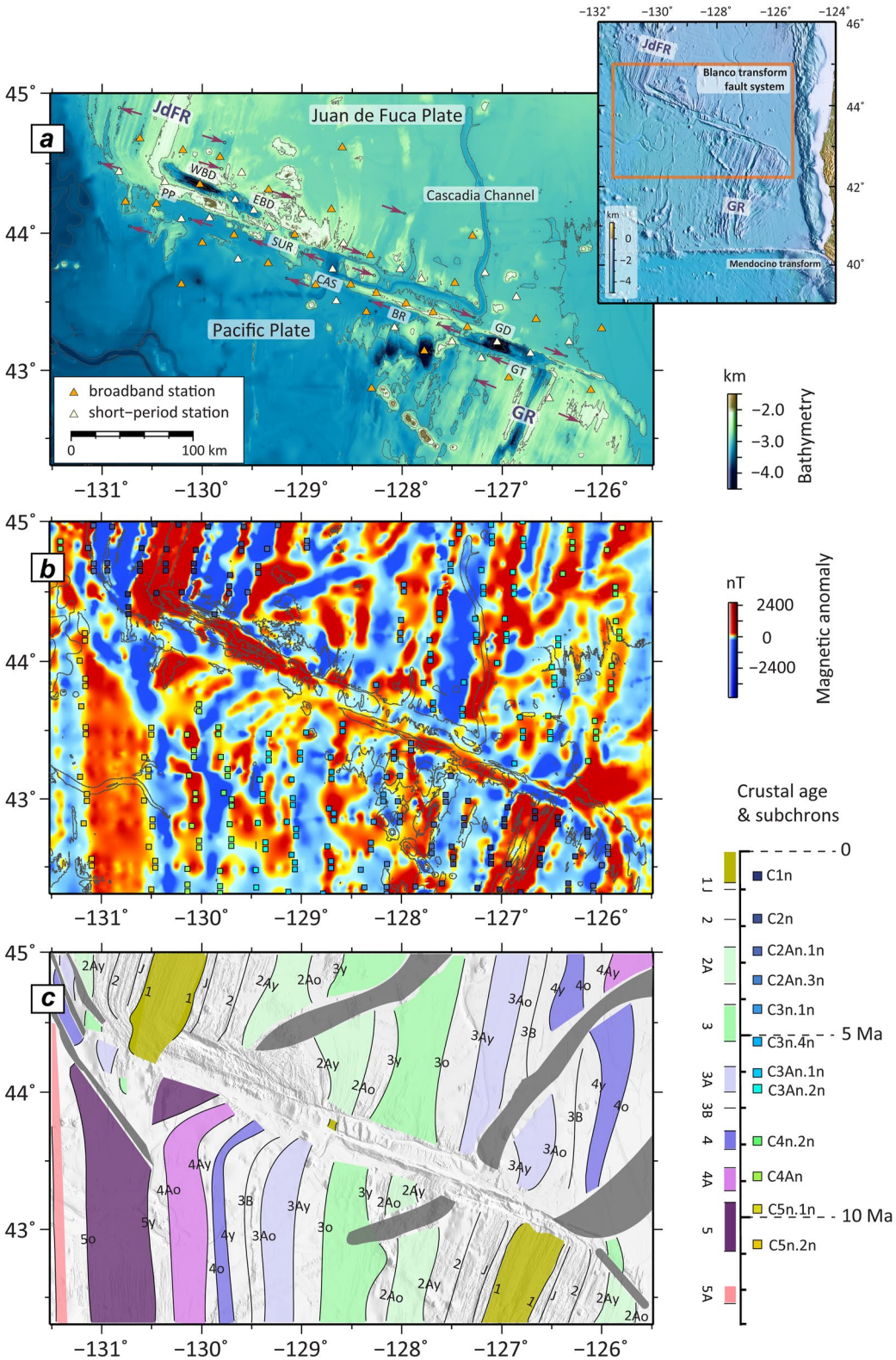

Figure 1.

shifted from the bathymetric features (e.g., Williams et al., 2019). The U.S. Navy's Sound Surveillance System (SOSUS) enabled earthquake detection using hydro-acoustic tertiary (T-) waves (e.g., Dziak et al., 2000, 2003; Géli et al., 2014), which significantly improved the precision of event locations. However, using the joint epicenter determination (JED) technique, Braunmiller and Nábělek (2008) suggested that the bathymetric features might bias the hydro-acoustic SOSUS locations along the BTFS, and that the lack of precise and accurate event locations put a limit on the identification of active faults, especially in the western BTFS.

The easternmost Gorda transform (GT) segment was identified from the bathymetric map (Embley & Wilson, 1992). Morphologically, from the intersection between the GR and GT, the linear fault trace extends northwestward ~20 km beyond the GD (Figure 1a). The GD is a ~20-km-long (trending NW-SE) and ~10-km-wide (trending NE-SW) basin with a central depth of ~4.4 km (Embley & Wilson, 1992). Troughs extend primarily to the southeast to the eastern ridge-transform intersection (RTI), into a region of negative magnetization (Figure 1b). The GD is bounded by the western GT and eastern BR transform segments. The 130-km-long BR connects the GD in the east and the CD in the west (Figure 1a), and it is the best-studied segment of BTFS to date. Braunmiller & Nábělek (2008) proposed that the eastern BR (east of 128°W) is fully coupled, due to the high seismicity combined with abundant relatively large events. Kuna et al. (2019) detected and located micro-earthquakes of the BR, and proposed a mode of slip at the BR where the fault zone in the crust is brittle and fully seismically coupled while in the mantle it creeps partially and episodically.

Located in the central BTFS, the CAS is an extensional basin bounded by the BR and SUR on the southern and northern sides (Figure 1a). A kinematic model by Embley and Wilson (1992) suggested that the CAS might be a remnant of a rift segment shortened due to a southward propagation event at ~5 Ma. Seismic reflection data revealed the presence of igneous intrusions within the sediments, suggesting the CAS is an intra-transform spreading center (Embley & Wilson, 1992). Furthermore, the CAS is seismically active (Johnson & Jones, 1978) and marked by normal faulting (Braunmiller & Nábělek, 2008).

From the northern boundary of the CAS, the fault trace extends to the southeast for around 120 km (Figure 1a), forming the southern scarp of the PP. To the northeast of the PP are three troughs (SUR, WBD, and EBD), marking the possible active tectonic features of the western BTFS. The SUR seems like a small pull-apart basin, as the northern and southern walls are discernible from seafloor morphology (Figure 1a). However, the master faults of EBD and WBD are difficult to interpret (Embley & Wilson, 1992), as many scarps are observed. The kinematic model of Embley and Wilson (1992) suggested that the western segment of BTFS was recently formed to accommodate far-field stress change.

Kuna et al. (2019) used micro-earthquake data collected during the Blanco Transform OBS Experiment in 2012, revealing depth-dependent seismic features of the BR. Yet, their study focused only on a regional subset sandwiched between the CD, which is an intra-transform spreading center, and the GD, interpreted as a pull-apart basin in the vicinity of the eastern RTI of BTFS. In addition, the whole seismic data set offers an excellent opportunity to improve our understanding of seismotectonic behaviors of the entire highly segmented oceanic transform system where most tectonic processes remain enigmatic.

3. Data and Methods

3.1. OBS Data

We use OBS data from the Blanco Transform OBS Experiment (Nábělek & Braunmiller, 2012). Fifty-five OBS were deployed between September 2012 and October 2013 (Figure 1a and Figure S2 in Supporting Information S1). Station BB270 did not record data, but all the other 54 OBS continuously recorded 100 samples per second. The average station spacing was approximately 25 km. Thirty-one stations were outfitted with broadband Güralp CMG3T seismometers, and the other 24 stations were equipped with short-period Mark Products L-28LB seismometers co-located with differential pressure gauges.

Figure 1. Tectonic map of the Blanco transform fault system (BTFS). (a) Bathymetry (Ryan et al., 2009) and ocean-bottom-seismometer (OBS) station distribution. Arrows show relative plate motion (DeMets et al., 2010) between the Pacific and Juan de Fuca Plates. The inset map shows prominent transform faults and fracture zones in the northeast Pacific. The colored box indicates the location of our study area. (b) Airborne magnetic anomaly (Bankey et al., 2002). Gray lines indicate the bathymetric contours with 600 m intervals. Color-coded squares show the magnetic picks from Elvers et al. (1973). (c) Crustal ages (modified from D. S. Wilson, 1993). Gray shading outlines propagator wakes (Nedimović et al., 2009). BR, Blanco Ridge; CAS, Cascadia Depression; EBD, East Blanco Depression; GD, Gorda Depression; GR, Gorda Ridge; GT, Gorda transform segment; JdFR, Juan de Fuca Ridge; PP, Parks Plateau; SUR, Surveyor Depression; WBD, West Blanco Depression.

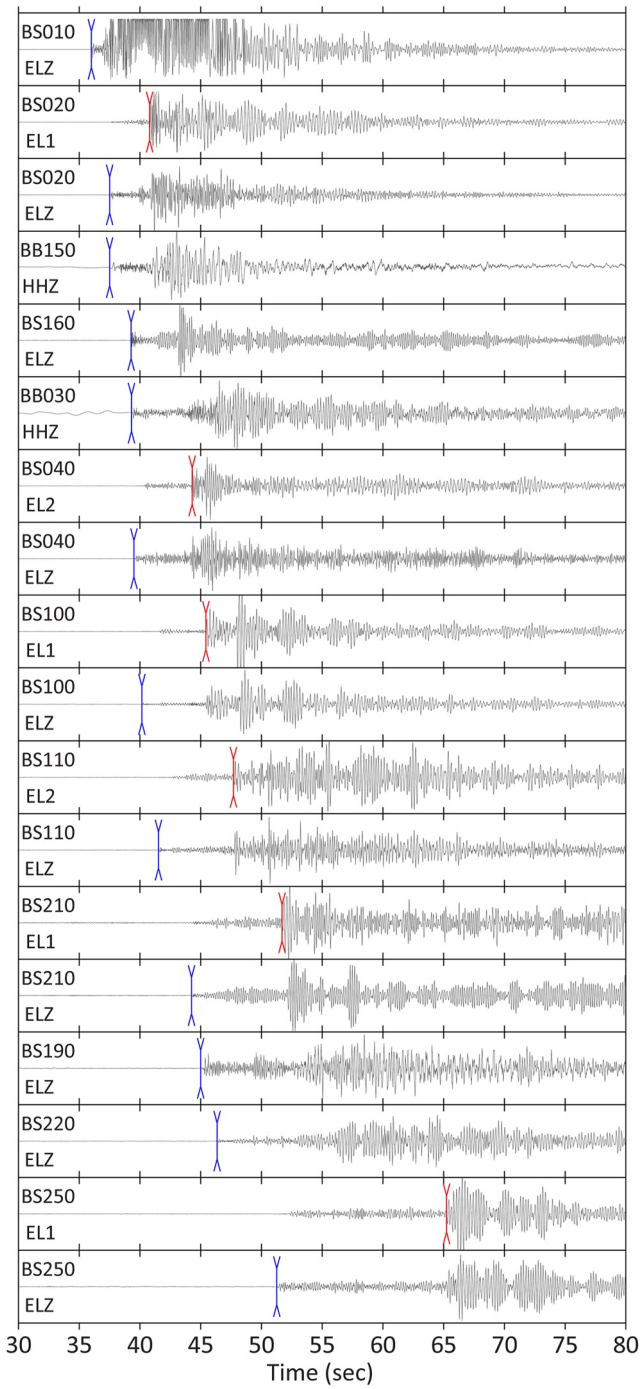

Figure 2. Seismograms of a local event recorded by the ocean-bottom-seismometer (OBS) array. The onsets of P-phase and S-phase arrivals are marked in blue and red, respectively. OBS labeled with "BS" and "BB" indicate short-period and broadband stations, respectively. The EL1 and EL2 represent horizontal channels; HHZ and ELZ stand for vertical channels.

3.2. Earthquake Catalog and Phase Picking

We constructed our seismicity catalog by combining the NEIC (National Earthquake Information Center) and an auto-detected catalog (Figure S3 in Supporting Information S1). The NEIC catalog listed 55 earthquakes between September 2012 and October 2013 along the BTFS. To enlarge our data set, we further applied automated event detection using the *scanloc* module of SeisComP3 (GFZ & Gempa GmbH, 2008). We selected 95 events with phase picks identified at more than 15 OBS stations to ensure the quality of earthquake locations. Interestingly, we found only six events from the auto-detected catalog are in common with the NEIC, supporting a recent observation that the auto-pickers might miss large magnitude events due to very emergent P-arrivals on OBS stations (Gong et al., 2022). Based on both catalogs, we constructed a new catalog with 144 events for earthquake relocation.

Furthermore, we revised the auto-picked phases and picked the NEIC events manually, as most NEIC events were not picked by the automated picker. Figure 2 depicts waveforms of a local event recorded by the OBS array. The onsets of P-phase and S-phase arrivals were manually picked on unfiltered waveforms. We picked P-phase onsets on the vertical channel and S-phase onsets on either one of the horizontal channels, where they are clearest. In total, 2,850 P-phases and 961 S-phases were picked for the determination of earthquake parameters.

3.3. Velocity Model, Event Location, and Magnitudes

Using VELEST (Kissling et al., 1994), we derived a minimum one-dimensional velocity model for the BTFS. We constructed 4,344 initial P-wave velocity models, which were inverted to find the model with the smallest RMS. This minimum 1D P-wave velocity model, with minimum RMS residuals among all output models, is shown in Figure 3. Then, we calculated the 1D minimum S wave velocity model by an additional iteration of inversions using different initial *Vp*/*Vs* ratios (e.g., Husen et al., 1999; Lange et al., 2007). Our minimum 1D velocity model is similar to the one Braunmiller and Nábělek (2008) used in their regional seismicity study utilizing coastal seismic stations (Figure 3), except for the slower P-wave velocity at 4–7 km depth. In the topmost layer within 1.5 km below the seafloor, P-wave velocity is estimated as ~4.6 km/s. P-wave velocities steadily increase from 5.7 to 6.3 km/s at depth between 1.5 and 7 km. At 7 km depth, the P-wave velocities increase from 6.3 to 7.6 km/s, which we interpret as the seismological Moho.

We used the non-linear oct-tree grid-search algorithm (NonLinLoc; Lomax et al., 2000) with the minimum 1D velocity models for *Vp* and *Vp*/*Vs* for event location. By the computation of probability density functions (PDFs) for each event, NonLinLoc allows estimations of location uncertainties. The maximum likelihood point of the complete non-linear location PDF was chosen as the preferred location. From the PDF scatter samples, uncertainties were estimated from 3D error ellipsoids fitted to each cloud of possible event locations. Uncertainties (68% confidence) in latitude, longitude, and depth are 0.5, 0.4, and 1.4 km, respectively. Furthermore, station correction terms (Husen et al., 1999) from NonLinLoc were calculated and iteratively updated to account for local velocity structures below the OBS network (Figure S4 in Supporting Information S1) (Grevemeyer et al., 2019). Finally, we located 138 local events (GAP<180°) with onsets from more than eight OBS stations, including at least one S-phase.

We further calculated local magnitudes (M_l) following Hutton and Boore (1987). The moment magnitudes (M_w) were manually estimated by the procedure described in Ottemöller and Havskov (2003). The M_l of

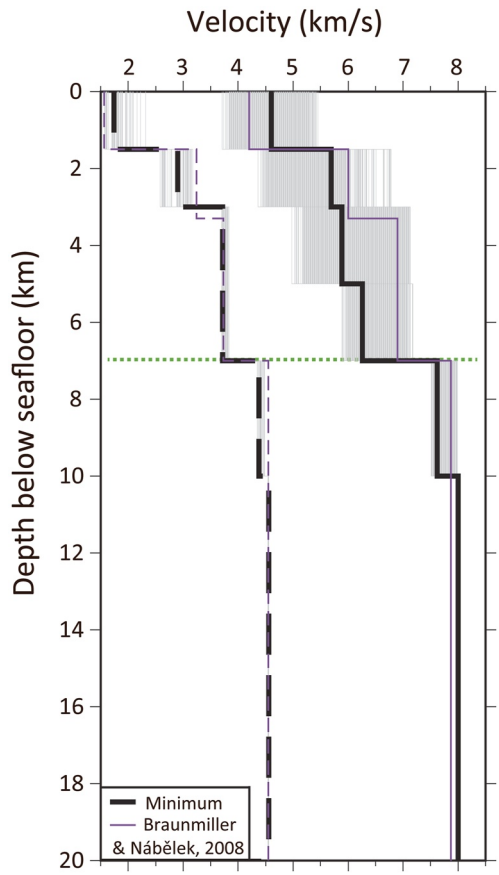

Figure 3. Minimum 1D velocity models of the Blanco transform fault system (BTFS). The P (black solid line) and S (black dashed line) wave velocity models were derived from 4,344 initial P-wave velocity models (gray lines). Solid and dashed purple lines show P-wave and S-wave velocity models used in previous regional seismicity study (Braunmiller & Nábělek, 2008), respectively. Dotted green line indicates the seismological Moho inferred from the minimum 1D velocity models.

nine events and the M_w of three events in our catalog are also listed in the NEIC (Figure S5 in Supporting Information S1). Our magnitudes deviate by −0.46 and 0.73 units from the NEIC values for the M_w and M_l, respectively.

3.4. Focal Mechanisms

We determined focal mechanisms for the events using their first motion polarities of P-phase onsets (Reasenberg & Oppenheimer, 1985). We retrieved focal mechanisms of 84 events with a GAP below 180° and first-motion polarities of P-phase onsets at more than 10 stations.

We also calculated the location bias of the seven events that are included in both gCMT (Ekström et al., 2012) and our catalogs (Figure S6 in Supporting Information S1). We obtain a bias of gCMT in latitude, longitude, and depth of 2.2, 1.1, and 7.9 km, respectively.

4. Results

The 1-year OBS deployment enabled us to depict the local seismicity (Figure 4 and Data Set S1) and focal mechanisms (Figure S7 in Supporting Information S1) along the entire BTFS with trustable location estimates (Figures S8 and S9 in Supporting Information S1). Our local seismicity catalog spans 12 months and includes 138 well-constrained events along the entire BTFS of local magnitudes (M_l) 1.7–4.9 and moment magnitudes (M_w) 1.9–5.2 (Figure S10 in Supporting Information S1). Our catalog is complete for all $M_l \geq 3.5$ events.

The seismicity distribution reveals a greatly improved correlation between the local earthquakes and the morphologic features along the BTFS (Figure 4). From the eastern intersection between the GR and the GT (Figure 5), earthquakes occurred following the fault trace (Figure 5), which formed the southern border of the GD. We show that the GD is seismically active, and normal faulting is observed within this deep basin, supporting that it is formed by extension or transtension (Braunmiller & Nábělek, 2008; Embley & Wilson, 1992). From the northern boundary of the GD to the CAS, local seismicity is also in-line with the structural lineament of the BR. The GD and BR are the most prominent tectonic features east of the CAS, sharing a similar focal depth range between 4 and 10 km depth, despite some deep events under BR and near the ridge-transform-intersection. The CAS is located at the mid-point of BTFS, connecting the eastern and western transform segments. Focal depth below CAS ranges from 4 to 10 km (Figure 6), similar to the eastern BTFS. To the west of CAS, three earthquake clusters occur at SUR, EBD, and WBD, respectively. The focal depth of the three earthquake clusters ranges consistently from 0 to 8 km (Figure 7). Most of the local events at the EBD occur in swarms (Figure S11 in Supporting Information S1).

Focal mechanisms derived in this study benefited significantly from the OBS deployment. Our local catalog includes 84 focal mechanisms with well-resolved event locations (Figures S7, S12, and S13 in Supporting Information S1), revealing the deformation styles of the highly segmented BTFS. The long-term near-field passive seismic observation enabled us to find that the major faulting style of the BTFS is strike-slip to transtensional rather than pure strike-slip (Figures S12 and S14 in Supporting Information S1). Moreover, seismic deformation varies locally along the entire segmented transform fault system. Dominantly strike-slip faulting is observed at the easternmost GT segment between the GD and the GR, including the vicinity of the RTI (Figure 5). The GD is dominated by normal faulting and extensional strike-slip motion. Along the BR, the primary faulting style is strike-slip to transtensional, except for one local event identified as reverse faulting (Figure 5). The CAS in the mid-point of the BTFS favors normal faulting in the central basin and transtensional strike-slip faulting near the BR and the SUR (Figure 6). However, faulting styles of the western BTFS are also quite similar, dominated by transtensional and strike-slip tectonics (Figure 7).

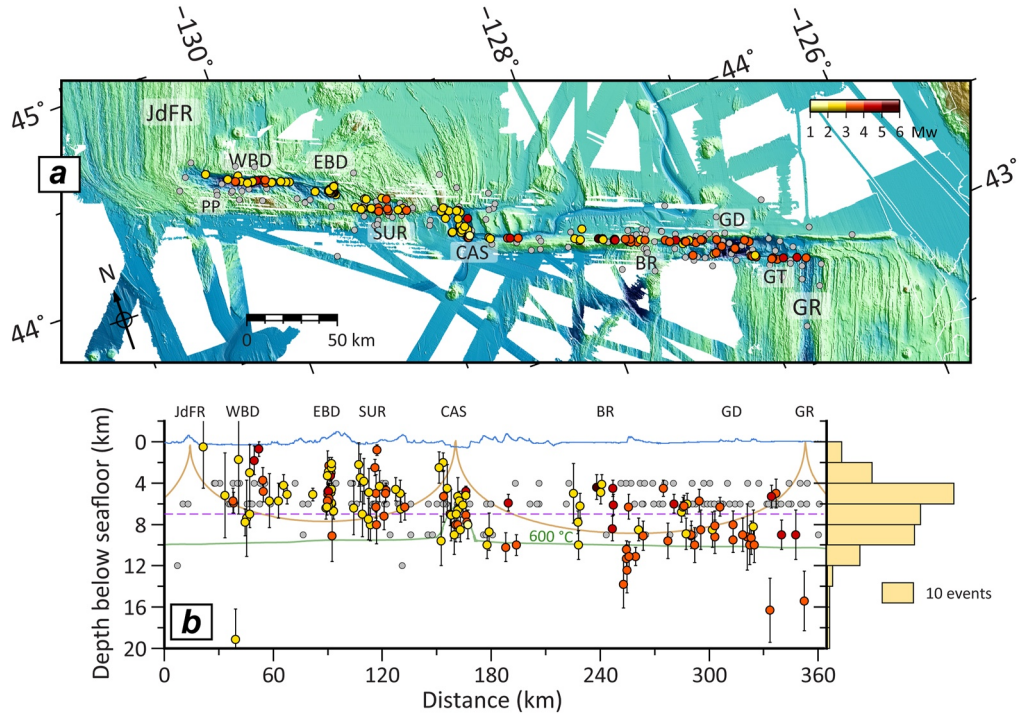

Figure 4. Distribution of local events (color-coded circles) along the entire Blanco transform fault system (BTFS). (a) Local seismicity of the BTFS. The gray circles show the hypocenters from Braunmiller and Nábělek (2008). (b) Along-strike vertical profile showing the focal depth distribution. Error bars indicate focal depth uncertainties (68% confidence). The light blue line shows the complexity of seafloor bathymetry. Dashed purple line shows the Moho discontinuity inferred from our minimum 1D velocity model. Brown and green lines indicate the 600°C isotherms calculated from a half-space cooling model and a numerical model incorporating hydrothermal cooling (Roland et al., 2010), respectively. Histogram on the right shows the focal depth distribution of local events derived in this study.

5. Discussion

The BTFS is a highly segmented OTF system. Morphologically, it is marked by deep troughs and bathymetry highs running along the fault traces (Embley & Wilson, 1992). According to the variation in regional seismicity (gray dots in Figure 4; Figure S12c in Supporting Information S1), Braunmiller and Nábělek (2008) categorized the complex fault system into four segments, namely GD, BR, Cascadia and Surveyor, and West Blanco segments. Three extensional basins (GD and Cascadia and Surveyor segments) and two transform segments (BR and West Blanco segments) were identified in their previous work. However, our local seismicity catalog suggests dividing the BTFS into five strike-slip or transfer segments (i.e., WBD, EBD, SUR, BR, and GT). We define transform segments as features dominated by strike-slip faulting, although some might also show minor dip-slip movement. In addition, three extensional basins (SUR, CAS, and GD) showing features resembling continental pull-apart basins (e.g., Aydin & Nur, 1982; Mann et al., 1983) might represent short intra-transform spreading centers (e.g., Fornari et al., 1989; Grevemeyer et al., 2013; Pickle et al., 2009), as long-lived extensional tectonics should favor the formation of new oceanic crust (van Wijk et al., 2017).

The eastern BTFS (Figure 5) consists of the BR and the GT as transform segments and the extensional basin GD. The CAS, located in the middle of the BTFS, is generally defined as a short spreading segment (Braunmiller & Nábělek, 2008; Embley & Wilson, 1992), but it also shows some characteristic features of a pull-apart basin (Figure 6). The western BTFS (Figure 7) includes three transform segments running along the SUR, EBD, and WBD (Figure 4). The SUR also shows pull-apart-basin-like features, bounded by two transform segments on its northern and southern sides. Detailed local seismicity, bathymetric, and aeromagnetic surveys reveal profound variations in seismotectonic behaviors along the entire BTFS, which will be discussed in detail below.

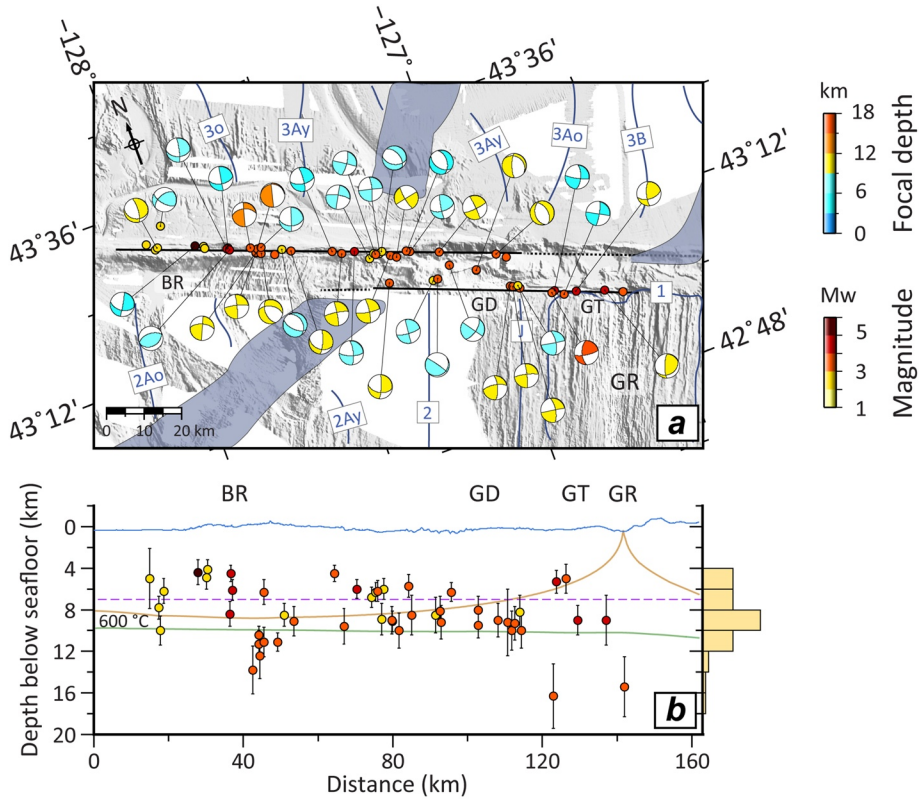

Figure 5. Close-up view of the eastern Blanco transform fault system (BTFS). (a) Local seismicity and focal mechanisms. Dark blue lines indicate the magnetic isochrons as in Figure 1c. Shaded polygons outline propagator wakes. Solid black lines show the interpreted transform fault traces. Dotted lines represent fracture zone traces identified from seafloor bathymetry. (b) Along-strike vertical profile showing the focal depth distribution. All other lines are as in Figure 4.

5.1. Local Seismicity and Tectonic Segments

5.1.1. Eastern Transform Segments

A number of multidisciplinary surveys were conducted to investigate the active tectonics of the eastern BTFS. The easternmost GT was identified from the bathymetry (Embley & Wilson, 1992). However, neither the hydro-acoustic T-wave events (Dziak et al., 2000) nor the JED locations (Braunmiller & Nábělek, 2008) could provide detailed seismological evidence for this active transform segment. However, we find that the local seismicity along the GT fits nicely with its fault trace observed morphologically, supporting the GT is an active transform fault segment bounding the southern side of GD (Figure 5). Near the RTI, earthquakes occurred close to the chron 1 (Brunhes magnetic chron) (Figure 5), indicating the seismotectonic behavior of the GT is related to recent magmatic activity since ~780 kyrs.

We observed seismic activity along both sides of the fault scarps of GT and BR (Figure 5). Previous seismicity studies (Braunmiller & Nábělek, 2008; Dziak et al., 2000) suggested that the fracture zone east of the GD might be seismically active, as a few events were identified (gray dots in Figure 4; Figure S12c in Supporting Information S1) using teleseismic analysis and/or JED technique. However, our local catalog shows that the seismicity didn't extend beyond the GD (Figure 5), indicating that the extending troughs and fracture zone east of the GD are aseismic. Furthermore, extensional strike-slip and normal faulting dominate this region, which is consistent with previous indications that the GD shows features of a pull-apart basin (Embley & Wilson, 1992). Alternatively, it may represent a rather magmatically starved short-spreading segment as found at the Mid-Atlantic Ridge at the Ascension (Grevemeyer et al., 2013) or in the southern segment of the Charlie Gibbs transform system (Skolotnev et al., 2021).

The occurrence of the BR as a prominent ridge-like structure represents a rare case as over 90% of OTFs revealed transform valleys instead of ridge-like morphology (Wolfson-Schwehr & Boettcher, 2019). Consistent

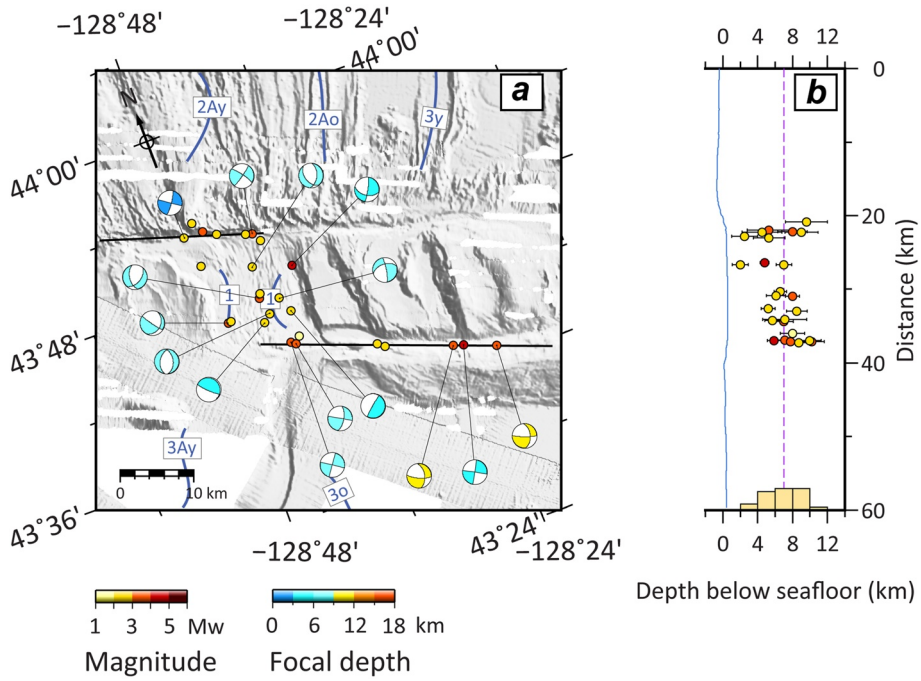

Figure 6. Close-up view of the Cascadia Depression (central Blanco transform fault system [BTFS]). (a) Local seismicity and focal mechanisms. (b) Vertical profile perpendicular to the strike of the BTFS showing the focal depth distribution. Symbols, lines, and labels are as in Figure 5.

with previous seismicity studies (Braunmiller & Nábělek, 2008; Dziak et al., 2000; Kuna et al., 2019), our results indicate that the seismic activity occurs along the BR (Figure 5), and that the seismicity of eastern BR is significantly higher than the western BR (west of 128°W) (Figures 5 and 6). Pockalny et al. (1997) suggested that such ridge-like features may form by compression caused by changes in plate motion. However, our seismic record provides little evidence to support such a scenario. As observed in our study (Figure 5), strike-slip and dip-slip faulting dominate the BR, supporting the proposed formation mechanism that simple shear motion with a small component of extension, which may have nurtured uplift along the fault (Dziak et al., 2000). Furthermore, a negative Bouguer anomaly over the BR (Dziak et al., 2000) may suggest that a low-density body, probably related to serpentine intrusions, caused further uplift of the BR. The occurrence of serpentinization in the mantle below the BR has also been inferred by Kuna et al. (2019) from the character of earthquakes and seismic swarms. The deviation from the characteristic valley-like morphology of OTFs (Grevemeyer et al., 2021; Wolfson-Schwehr & Boettcher, 2019) may suggest that the BR has not yet established its final structure.

5.1.2. Cascadia Depression

The CAS is seismically active (Johnson & Jones, 1978), and marked by normal faulting (Braunmiller & Nábělek, 2008). Consistently, we also observe normal faulting dominating the axis of the CAS (Figure 6), supporting it is a spreading segment (Braunmiller & Nábělek, 2008; Embley & Wilson, 1992). Strike-slip events close to the spreading axis might be related to magma movement. The transtensional strike-slip faulting observed near both ends of the short spreading segment indicates the transition from transform shear stress to tensile ridge axis stress. The focal depth ranges primarily from 4 to 10 km below seafloor, fitting into the focal depth ranges of mid-ocean ridge seismicity (Grevemeyer et al., 2019), suggesting that the magma source is deep. A positive magnetization (Figure 1b) supports the occurrence of the chron 1 (Brunhes magnetic chron) along the short spreading axis (Figure 6a), supporting magma-poor spreading at the CAS.

5.1.3. Western Transform Segments

The western segments reveal the most complex tectonic structures within the BTFS (Embley & Wilson, 1992). Active faults are hard to interpret (Embley & Wilson, 1992) as too many scarps are observed near the bathymetric

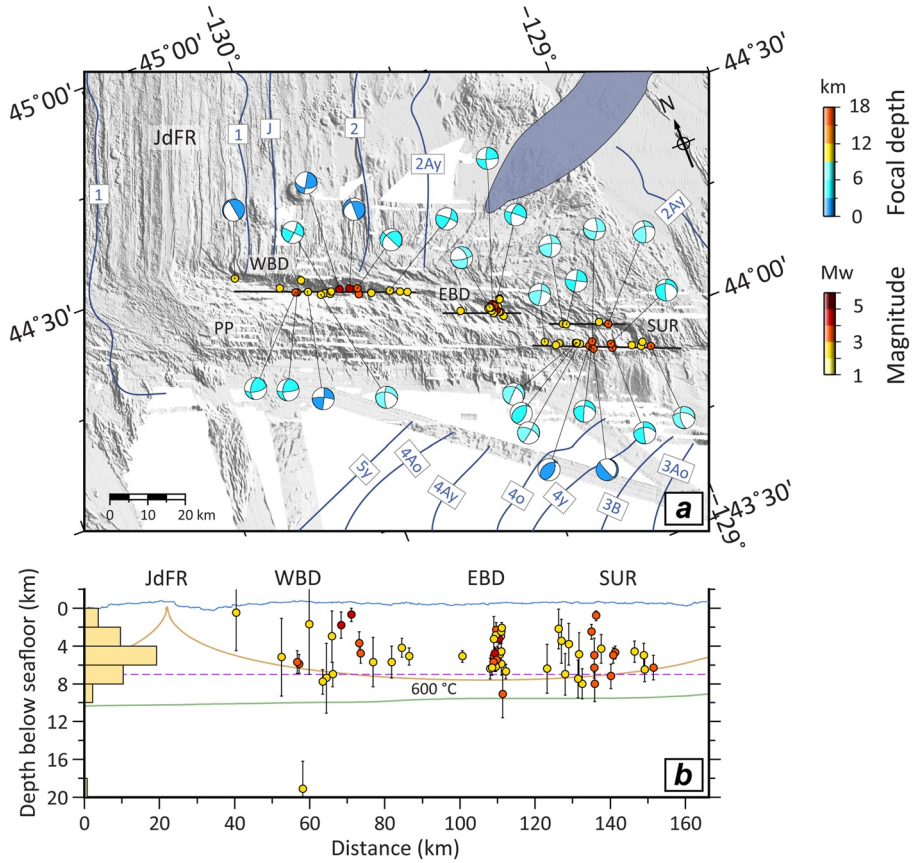

Figure 7. Close-up view of the western Blanco transform fault system (BTFS). (a) Local seismicity and focal mechanisms. (b) Along-strike vertical profile showing the focal depth distribution. Symbols, lines, and labels are as in Figure 5.

features (i.e., PP, WBD, EBD, and SUR). The kinematic model of Embley and Wilson (1992) suggested that the western BTFS was recently formed to accommodate far-field stress change. They speculated the main transform motion had been shifted from the PP to its northeastern troughs and each lineation on the seafloor might be an active fault. Dauteuil (1995) performed a more detailed bathymetric analysis, supporting the existence of a recent jump of the western transform plate boundary and a 15° rotation of the active direction. However, most OTFs generally run along prominent valleys (Ren et al., 2022; Wolfson-Schwehr & Boettcher, 2019), and therefore, it is difficult to understand which processes should have caused a prominent volcano-like feature.

Unfortunately, routine teleseismic event locations along the BTFS are scattered and systematically shifted from the bathymetric features (e.g., Dziak et al., 1991). With significantly improved precision, hydro-acoustic T-wave locations (Dziak et al., 2003; Géli et al., 2014) observed seismic activity near the northern boundary of PP and the southern wall of WBD. However, Braunmiller and Nábělek (2008) doubted the location uncertainties of the hydro-acoustic locations, which might involve systematic biases. In addition, they claimed that their relocated events are too scattered to identify the active faults of the western BTFS (Braunmiller & Nábělek, 2008).

Our results reveal for the first time the stress patterns of local seismic activity along the western BTFS, coinciding with bathymetric features (Figure 7). Between the WBD, EBD, and SUR, seismicity is sparse. At the SUR, two strands of earthquakes align well with the northern and southern walls identified from seafloor morphology, providing robust evidence for the exact location of active faults (Figure 7) and hence can be interpreted as pull-apart tectonics dominated. At the EBD, seismic activity was sparse during the OBS deployment, except for an earthquake swarm from October 2 to 3, 2012 (Figure 7 and Figure S11 in Supporting Information S1). Seismicity along the adjacent WBD occurs in the deepest parts of the central valley, with one extensional event on the northern wall, indicating tectonic extension near the RTI. Therefore, the WBD shows characteristic features on OTFs (Grevemeyer et al., 2021; Ren et al., 2022), while the SUR and EBD are short segments and comparable

to non-transform offsets (e.g., Macdonald et al., 1988). Although the SUR shows similar pull-apart features in seafloor morphology, like the CAS and GD, it is worth noting that the SUR does not show typic seismological pull-apart features as no extensional faulting occurred within the central basin and instead reverse faulting is notable (Figure 7a). Furthermore, the PP is an aseismic tectonic feature, suggesting that the active transform plate boundary runs northward of PP.

5.2. Focal Depth and Thermal Structure of the Eastern and Western Transform Segments

Most previous seismicity studies of the BTFS (e.g., Dziak et al., 2003; Géli et al., 2014) did not provide focal depth determination except for the JED event locations procedure of Braunmiller and Nábělek (2008) and the microseismicity survey along the BR (Kuna et al., 2019). Braunmiller and Nábělek (2008) suggested that focal depths near RTIs are slightly shallower (4–6 km) than in the central transform system (4–9 km) (Figure 4). In contrast, our local seismicity distribution does not support their observation. We observed deep events near the RTIs exceeding 14 km (Figure 4), which were also noticed by a recent microseismicity study of the eastern RTI of the Romanche transform fault (Yu et al., 2021). More interestingly, focal depths of the eastern BTFS are systematically deeper (4–10 km) than those of the western BTFS (0–8 km) (Figures 5 and 7), suggesting different modes of slip at the eastern and western segments of the BTFS. To constrain the maximum depth of faulting, we further extracted the 600°C isotherms (Figures 4, 5, and 7) from a half-space cooling model and a geodynamic model incorporating hydrothermal cooling (Roland et al., 2010).

At the eastern BTFS (Figure 5), more than half of the earthquakes occurred in the uppermost oceanic mantle below 8 km. The other crustal events peak between 4 and 7 km, indicating an aseismic upper oceanic crust. Between 7 and 8 km in depth, it seems to be a 1-km-wide aseismic band around at Moho depth, which was first observed by Kuna et al. (2019). Hydrothermally altered gabbros, diabases, and basalts were dredged from the site between the GD and the BR, supporting active hydrothermal fluid activity at the eastern BTFS (Hart et al., 1990). Therefore, hydrothermal cooling is a critical process affecting the thermal structure of this region (Roland et al., 2010). The local events are mostly constrained by the 600°C isotherm from the hydrothermal cooling model (green lines in Figures 4 and 5), except for a cluster of deep events at the central BR and two events below 14 km near the GR. Braunmiller and Nábělek (2008) suggested the eastern BTFS seems fully coupled; thus, the relative plate motion accounted for brittle deformation in the lower crust and uppermost mantle of the eastern BTFS. The existence of serpentinite peridotite in the uppermost mantle (Dziak et al., 2000; Embley & Wilson, 1992; Kuna et al., 2019) might result in the velocity-strengthening mode that inhibits earthquake nucleation of the upper crust (0–4 km) (Boettcher & Jordan, 2004). Furthermore, deep earthquakes (higher than 600°C) up to ∼16 km were observed at central BR and near GR, supporting the semi-brittle deformation in the mantle (Prigent et al., 2020; Yu et al., 2021).

In contrast, at the western BTFS (Figure 7), most events occurred in the oceanic crust (0–8 km). Like the eastern segment, the 600°C isotherm from the hydrothermal cooling model limits the depth of seismicity and brittle faulting, as Roland et al. (2010) predicted. Compared to the fully coupled eastern BTFS, we suggest a different seismotectonic behavior of the western BTFS; thus, relative plate motion is accommodated mainly via brittle deformation shallower than the 600°C isotherm, while creep dominates in the uppermost mantle.

5.3. Two End-Members of Ridge-Transform Interaction

RTIs endure the most prominent interaction between transform faults and the truncated spreading segments, representing the transition from transform shear stress to tensile stress (Distortions, 1989; Morgan & Parmentier, 1984). Furthermore, RTIs show prominent features, including J-shaped ridges, hummocks, and small volcanic cones extending across the RTI, often covering the outside corner-fracture zone region terminating in the older plate (Grevemeyer et al., 2021). These J-shaped ridges appear to be formed by the progressively oblique prolongation of the adjacent spreading axis across the transform fault.

Here, we observe different types of morphologic features at the western and eastern RTIs as well as along the transform domains. J-shaped ridges occur at both RTIs but are much more prominent at the western RTI where the JdFR surpasses the WBD and curves into the PP (Figures 1a and 7a), indicating that the PP may represent a "rooster comb" as observed at a number of fast spreading OTF. Thus, at the East Pacific Rise, J-shaped ridges are often associated with shallower bathymetry (rooster combs) where the older lith-

osphere and the opposing ridge tip are juxtaposed (Barth, 1994; Fornari et al., 1989; Gallo et al., 1986). As a result, the adjacent WBD shows typical OTF features, running along a deep valley with tectonic extension (Grevemeyer et al., 2021; Ren et al., 2022). However, at the eastern RTI, the northern GR is truncated by the GT, and the J-shaped ridges occur, but do not run across the deep GD (Figures 1 and 5a). Furthermore, the negative magnetic anomaly north to the truncated GR suggests that its seabed was formed before the chron 1 (Brunhes magnetic chron) at least 780 kyrs ago (Figures 1 and 5a), which supports a lack of recent magmatic activity near this region and a weak interaction between the GR and the eastern BTFS. Although both RTIs show characteristic features of OTFs, it is reasonable to suggest that the impact of spreading episodes of the adjacent spreading ridges on the transform faults is weaker in the east than in the west, resulting in a different mode of slip at the western and eastern BTFS.

5.4. Evolution of the BTFS Revisited

Structurally, the BTFS shows strong similarities with other segmented OTFs in the Pacific, like the Siqueiros transform system on the East Pacific Rise (Fornari et al., 1989). At the Siqueiros transform, a documented change in spreading direction caused a single transform fault to be subjected to a series of extensional events that led to the formation of an intra-transform spreading segment (Pockalny et al., 1997). The configuration of the BTFS also resulted from plate reorientation at ∼5 Ma (Embley & Wilson, 1992). However, the BTFS developed from at least two transform faults (Embley & Wilson, 1992) or non-transform ridge offsets (Cowan et al., 1986; McKenzie, 1986; D. S. Wilson, 1990) rather than from a single transform fault. The CAS in the central BTFS, an intra-transform spreading center observed today, is a remnant of a rift segment shortened due to a series of rift propagation events (Embley & Wilson, 1992) instead of extensional events as described at the Siqueiros transform (Pockalny et al., 1997).

However, we have little evidence for stable transform faults at ∼5 Ma as envisioned by Embley and Wilson (1992). In plate tectonics, fracture zones mark the inactive trace of a transform fault (Grevemeyer et al., 2021; Morgan, 1968); hence, any mature transform fault should leave an adjacent fracture zone. However, seafloor morphology (Figure 8) does not provide evidence for fracture zone traces issuing from the westernmost BTFS, indicating that the western segment represents an immature transform system. In contrast, at the eastern BTFS fracture zone, traces of the BR and the GT extends 80 and 30 km to the east and the west of the GD, respectively (dotted lines in Figure 8), suggesting the BR and GT are reasonably mature features. Furthermore, if we idealize that the slip rate is constant (49 mm/yr; DeMets et al., 2010), the initial formation of the BR and GT could be traced at ∼1.6 and ∼0.6 Ma, respectively. Bathymetric and gravity data (Figure 8 and Figure S1 in Supporting Information S1; Matthews et al., 2011) provide no regional evidence of any transform fault or fracture zone between the JdFR and GR before 2 Ma. Therefore, we support the interpretation that the evolution of the BTFS was primarily controlled by ridge propagation (D. S. Wilson, 1993; Wilson et al., 1984) and hence the reorientation of non-transform offsets rather than discrete transform faults as depicted by Embley and Wilson (1992).

Ridge propagation is a temporary phenomenon and inconsistent with simple strike deformation (McKenzie, 1986). The migrating ridge tip may cause a large domain of bookshelf faulting between the propagator and the opposing "doomed" ridge (McKenzie, 1986; Morgan & Kleinrock, 1991), which has also been observed at the Sovanco transform deformation zone linking the northern JdFR and the southern Explorer Ridge (Cowan et al., 1986). We therefore revised the kinematic model of the BTFS (Figure 9), by replacing the simplified discrete transform model (Embley & Wilson, 1992; D. S. Wilson, 1988) with the broad transform zone model (McKenzie, 1986; Morgan & Kleinrock, 1991; D. S. Wilson, 1990) for rift propagation. We suggest that broad transform zones (i.e., bookshelf faulting domains) linked the propagating JdFR and GR before ∼5 Ma (Figure 9a). In response to the clockwise shift in the Juan de Fuca/Pacific pole of rotation at ∼5 Ma (D. S. Wilson, 1993), the bookshelf faulting domain and the ridge segments rotated clockwise, except that the eastern rift segment roughly remained geographically anchored (Embley & Wilson, 1992; Figure 9b). As a result, the ridge segment in the middle was shortened (Figure 9b). Furthermore, a series of ridge propagation events (Embley & Wilson, 1992; D. S. Wilson, 1993) contributed to the complexity of the entire BTFS. The southward propagation of the JdFR integrated two transform deformation zone by eliminating the ridge segments in between, while the northward propagation of the GR attached a small transform deformation zone in the easternmost and shortened the

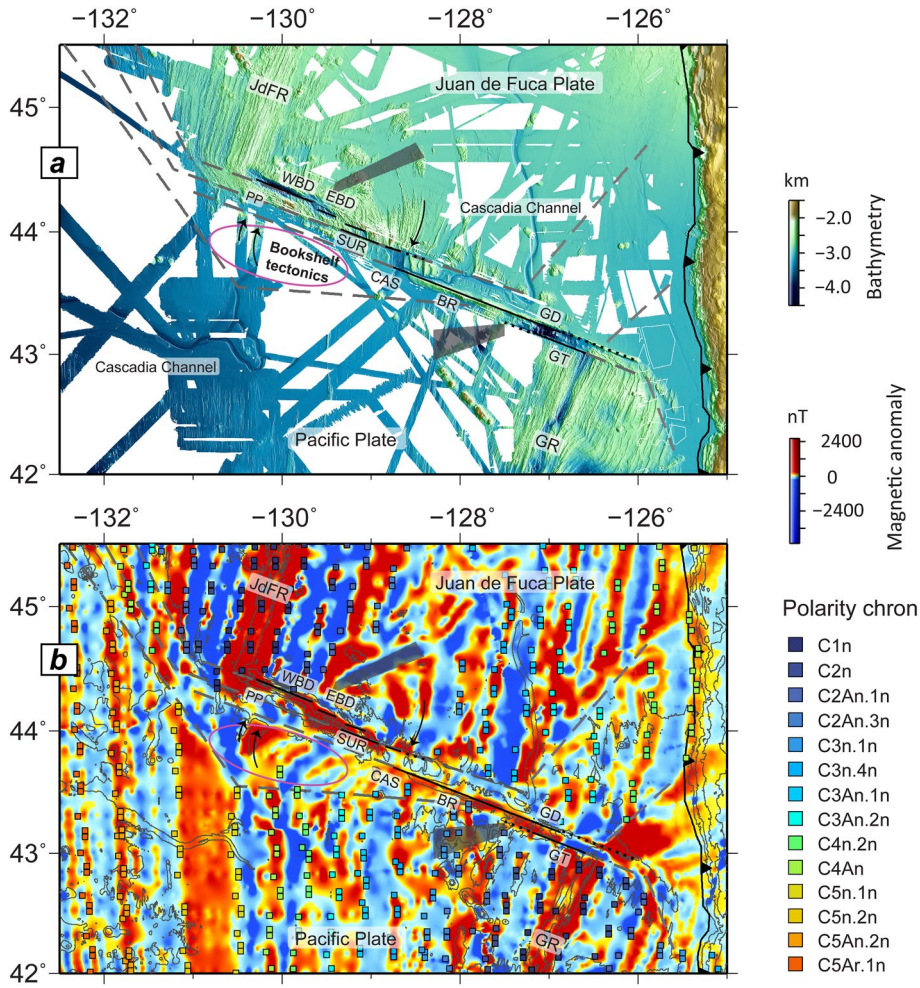

Figure 8. Tectonic interpretation of the Blanco transform fault system (BTFS). Solid black lines show active transform plate boundaries of the BTFS. Dotted lines show fracture zone traces. Dashed lines indicate the pseudofault traces in response to rift propagation and plate rotation. Shaded polygons outlined the narrow zone of the inner-pseudofault and failed rift suggested by D. S. Wilson (1990). Magnetic polarity time scale is as in Figures 1b and 1c.

doomed segment in the north (Figure 9c). At small offsets, the inward jumps of the failed rift cut across the inner-pseudofault into the material formed at the propagator (D. S. Wilson, 1990), which has been marked in the inside corners of the BTFS (Figure 8). Both propagation events of the JdFR and the GR stopped before ∼1.8 Ma (Figure 8; D. S. Wilson, 1993), and thereafter the relative plate motion between the Juan de Fuca and Gorda Plates became reasonably stable. After the propagation events, ridge-transform interaction accounted primarily for the nucleation of active transform faults (e.g., Gerya, 2012). In the eastern BTFS, the northward propagation of GR stopped ∼10 km before reaching the BR deformation zone (Embley & Wilson, 1992), hence the formation of the GD and its extending troughs north to the GR (Figure 9d). The BR and the GT became mature transform faults with the growth of fracture zones since ∼1.6 and ∼0.6 Ma, respectively (Figure 9d). South to the PP, rotated crustal features are notable (highlighted in Figure 8), supporting the rotated bookshelf faulting domain of the BR in response to plate rotation has been transported to the northwest due to seafloor spreading (Figure 9). However, unlike the intra-transform spreading centers CAS and GD, the SUR in the west BTFS does not show typical pull-apart feature, as no extensional faulting was observed within the deep basin (Figure 7a). We suggest that the EBD and SUR are remnant features developed from doomed ridge segments (Embley & Wilson, 1992) that already died during propagation (Figure 9e), leading to ongoing reorganization to accommodate relative plate motion.

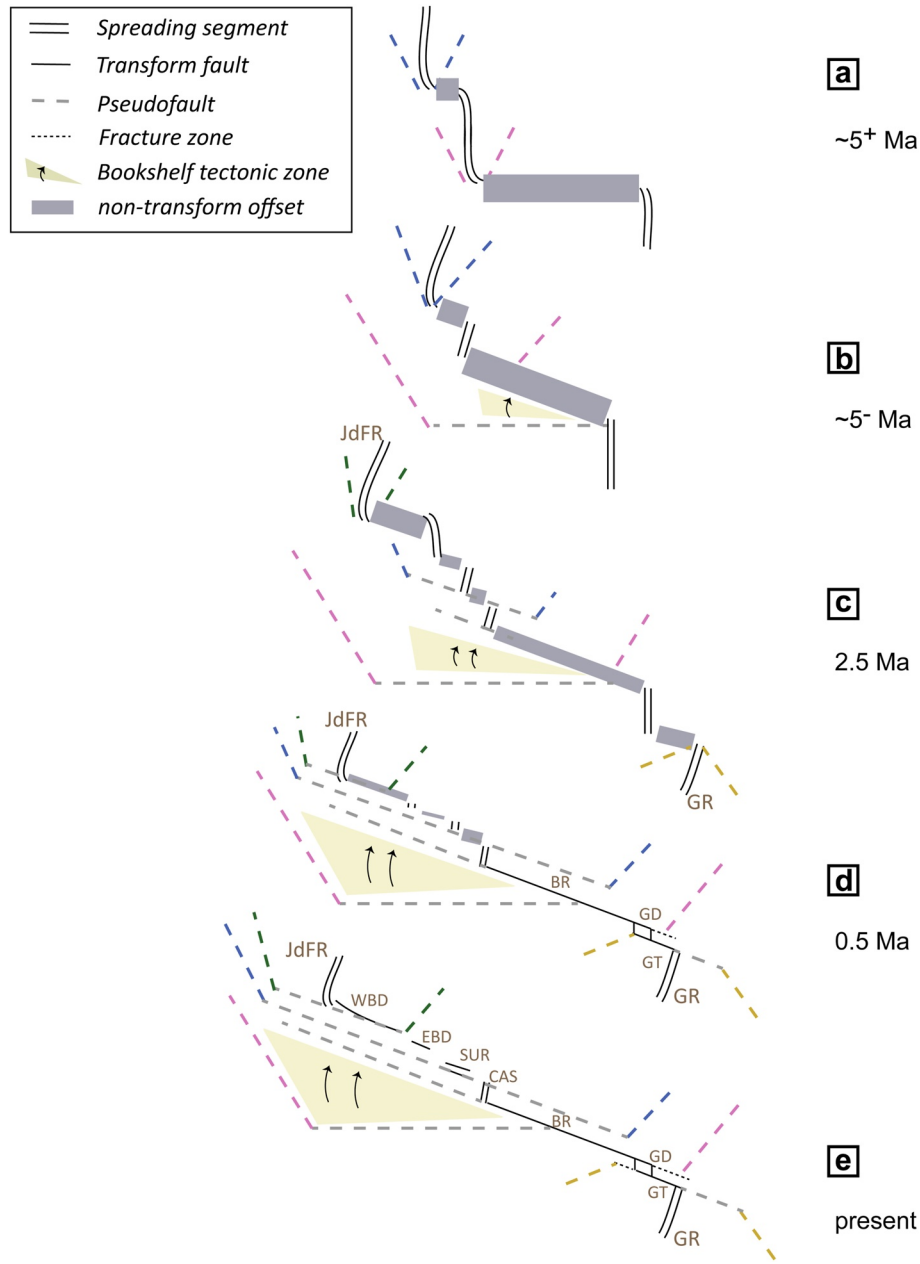

Figure 9. Development of transform faults and ridge segments since the formation of the Blanco transform fault system at around 5 Ma due to the clockwise shift in the Juan de Fuca/Pacific pole of rotation. Modified from Embley and Wilson (1992).

Relative azimuths between slip vector azimuths from focal mechanisms constrained by the OBS network and plate motion azimuths from MORVEL (DeMets et al., 2010) (Figure 10) support the scenario outlined above. As discussed, the pseudofault traces of the most recently active propagating rifts are identifiable at the inside corners from the airborne magnetic anomaly map (Figure 1), reaching the BTFS before chron 2 (~1.86 Ma) (D. S. Wilson, 1993). Therefore, it is indicated that no significant plate rotation has occurred around the BTFS over the past 1.8 Ma, allowing a meaningful comparison between slip vector azimuths from local events and the plate motion azimuths that are averaged over the past 780 kyrs (DeMets et al., 2010). We observed systematic variations in the relative azimuths, which seem to decrease from west to east along the entire BTFS (Figure 10c). The transform segments in the west and the CAS show mostly positive values (i.e., clockwise skewed). At the same time, the relative azimuths are scattered about the trend of plate motion in the east

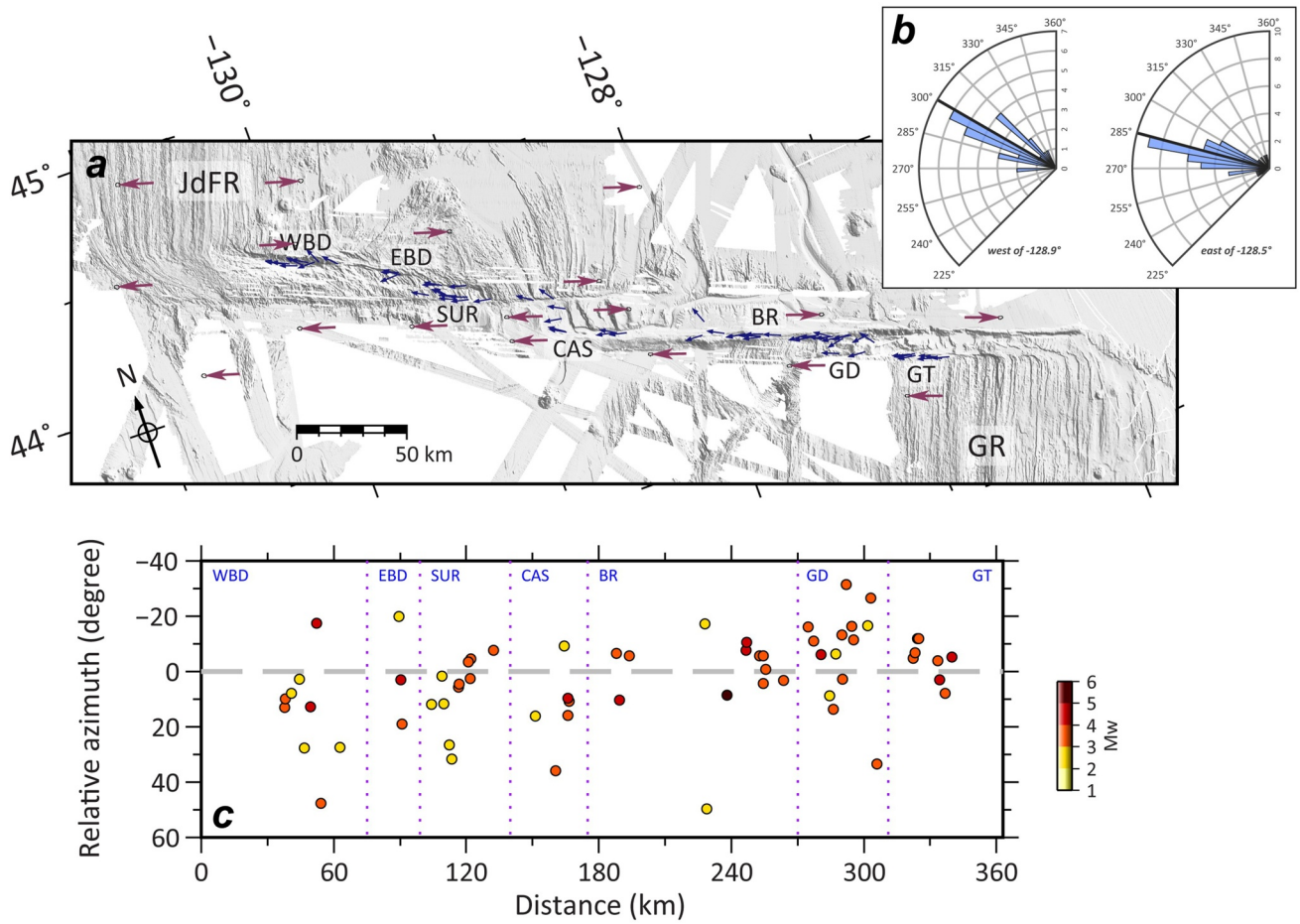

Figure 10. Strain partitioning at the Blanco transform fault system (BTFS). (a) Slip vector derived from 84 focal mechanisms. The blue and brown arrows indicate slip vectors from focal mechanisms and relative plate motion azimuths (DeMets et al., 2010) between the Pacific and Juan de Fuca Plates, respectively. (b) Rose diagrams of slip vector azimuths. The observed azimuths are binned in 5° intervals, and the solid black lines indicate the median azimuths of the western and eastern segments of the BTFS. (c) Variations of slip vector azimuths plotted relative to the plate motion azimuths from DeMets et al. (2010).

segment, though slightly negative values dominate. Therefore, stresses at the eastern segments, which established at ~0.6 Ma, roughly mimic plate motion, while the younger western segment may still adjust to the new stress regime.

Distributions of local events, strain partitioning, bathymetric features, magnetic data, and the tectonic evolution of the BTFS can be better interpreted in terms of two OTF systems instead of a single transform fault system. The CAS would represent the tectonic boundary separating both OTFs. The eastern BTFS is a relatively mature OTF system which was established at ~0.6 Ma, suggested to be highly coupled (Braunmiller & Nábělek, 2008; Kuna et al., 2019), and plate motion is mainly accommodated by brittle deformation in the lower crust and uppermost mantle (4–10 km). In contrast, the western BTFS emerged after a series of ridge propagation events stopped at ~2 Ma. However, in the recent geological past, it has been affected by typical tectonic extension at OTFs (Furlong et al., 2001; Grevemeyer et al., 2021), causing the formation of deep troughs along the active WBD, which is in line with the observation that OTFs commonly run along deep valleys (Ren et al., 2022). Plate motions at the western BTFS are accommodated mainly by brittle deformation at temperatures below 600°C (0–8 km) and creep in the mantle. The clockwise skewed stresses of the western BTFS (Figure 10) suggest that the recent reorganization of the west segments (Braunmiller & Nábělek, 2008; Embley & Wilson, 1992) might still be active in the near future.

6. Conclusions

One year of local seismic activity recorded along the entire BTFS enabled us to reveal the local seismicity and focal mechanisms within a 350-km long and strongly segmented OTF system. Based on high-quality hypocenters of local seismicity together with bathymetric, magnetic, and gravity data sets, we revised the kinematic model of the BTFS for the last ~5 Ma. Our results suggest that:

1. Local events align perfectly with morphologic features of the BTFS, indicating the active transform plate boundaries consist of the GT segment, BR, two strike-slip fault strands of the SUR, EBD, and WBD.
2. In the eastern BTFS, stresses are mainly accommodated by brittle deformation in the lower crust and uppermost mantle (4–10 km below the seafloor). In contrast, plate motions at the western BTFS are accommodated primarily by brittle deformation at temperatures below 600°C (0–8 km) and creep in the mantle. Deep earthquakes were also observed near the RTIs and the BR, inferring semi-brittle deformation.
3. Seafloor bathymetry reveals magma-robust features and J-shaped ridges surpassing the transform valley at the western RTI. However, at the eastern RTI, magma-poor features as well as truncated J-shaped ridges which stopped at the GD are observed. These different behaviors corresponding to strong and weak ridge-transform interaction, respectively, might account for the along-strike variation of the BTFS.
4. Consistent with gravity field data, there is no clear trace of fracture zone of the BTFS, except for the newly developed fracture zones adjacent to BR and GT. We therefore exclude the existence of fracture zones or established transform faults of the BTFS before 2 Ma. Accordingly, our modified kinematic model suggests the BTFS developed from a number of broad transform deformation zones (Cowan et al., 1986; D. S. Wilson, 1990) linking ridge segments during rift propagation events before ~2 Ma, rather than discrete transform faults suggested by Embley and Wilson (1992);
5. The BR and GT of the eastern BTFS were formed at ~1.6 and ~0.6 Ma, respectively. Although the EBD, SUR, CAS, and GD developed from ridge segments during the propagation events of the JdFR and GR, different seismotectonics of each segment suggest the CAS and GD are intra-transform spreading centers, while neither EBD nor SUR is corresponding to the formation of oceanic crust, representing remnant features of doomed rifts that already died during propagation.
6. Seismic slip vectors reveal that stresses in the eastern BTFS roughly coincide with the direction of plate motion, suggesting a mature transform fault system accommodating the plate motion. However, stresses to the west are clockwise skewed, indicating the re-organization of the western BTFS is still active now.
7. Multidisciplinary observations support different seismotectonic behaviors of the western and the eastern BTFS, suggesting that the BTFS could be divided into two oceanic transform systems impacted by two end-members of ridge-transform interaction. The eastern BTFS became a mature transform plate boundary since ~0.6 Ma. Although the westernmost WBD near the RTI shows the typical oceanic transform feature that active faults run along deep valleys, the other segments further away from the RTI may still develop over time. We therefore suggest the western BTFS is an immature transform system, which has been continually evolving to accommodate far-field stress change.

Acknowledgments
Our study benefitted from GEOMAR's OCEANS program. Yu Ren was supported by the China Scholarship Council (Grant 201904910466) and the 2022 Beacon Prize sponsored by Zhihu Incorporation. The authors thank all persons who contributed to data collection in the Blanco Transform OBS experiment (Nábělek & Braunmiller, 2012). Seismic data used in this study, which are archived at the IRIS Data Management Center (http://www.iris.edu), were provided by instruments from the Ocean Bottom Seismic Instrument Center (https://obsic.whoi.edu/). This manuscript benefitted from conversations with Jason P. Morgan, Colin Devey, Lars Rüpke, Sibiao Liu, and Zhikui Guo. The authors thank editor Isabelle Manighetti, associate editor, Milena Marjanović, and an anonymous reviewer for their thoughtful comments and efforts toward improving this manuscript. Open Access funding enabled and organized by Projekt DEAL.

Data Availability Statement

The continuous seismological data are accessible from the IRIS under the network code X9 (2012–2013; https://doi.org/10.7914/SN/X9_2012). Bathymetric data are available via https://www.gmrt.org/GMRTMapTool/. Airborne magnetic anomaly data are available from the USGS Mineral Resources Program (https://mrdata.usgs.gov/magnetic/).

References

Atwater, T., & Stock, J. (1998). Pacific-North America plate tectonics of the Neogene Southwestern United States – An update. *International Geological Review*, *40*(5), 375–402. https://doi.org/10.1080/00206819809465216

Aydin, A., & Nur, A. (1982). Evolution of pull-apart basins and their scale independence. *Tectonics*, *1*(1), 91–105. https://doi.org/10.1029/TC001i001p00091

Bankey, V., Cuevas, A., Daniels, D., Finn, C., Hernandez, I., Hill, P., et al. (2002). Digital data grids for the magnetic anomaly map of North America. USGS Open File Report 2002-414. https://doi.org/10.3133/ofr02414

Barth, G. A. (1994). Oceanic crust thickens approaching the Clipperton Fracture Zone. *Marine Geophysical Researches*, *16*(1), 51–64. https://doi.org/10.1007/BF01812445

Boettcher, M. S., & Jordan, T. H. (2004). Earthquake scaling relations for mid-ocean ridge transform faults. *Journal of Geophysical Research*, *109*(B12), B12302. https://doi.org/10.1029/2004JB003110

Braunmiller, J., & Nábělek, J. (2008). Segmentation of the Blanco Transform Fault Zone from earthquake analysis: Complex tectonics of an oceanic transform fault. *Journal of Geophysical Research*, *113*(B7), B07108. https://doi.org/10.1029/2007JB005213

Carbotte, S. M., Nedimović, M. R., Canales, J. P., Kent, G., Harding, A., & Marjanović, M. (2008). Variable crustal structure along the Juan de Fuca Ridge: Influence of on-axis hot spots and absolute plate motions. *Geochemistry, Geophysics, Geosystems*, *9*(8), Q08001. https://doi.org/10.1029/2007GC001922

Carbotte, S. M., Smith, D. K., Cannat, M., & Klein, E. M. (2015). Tectonic and magmatic segmentation of the Global Ocean Ridge System: A synthesis of observations. In T. J. Wright, A. Ayele, D. J. Ferguson, T. Kidane, & C. Vye-Brown (Eds.), *Magmatic rifting and active volcanism* (Vol. 420, pp. 249–295). Geological Society. https://doi.org/10.1144/SP420.5

Cowan, D. S., Botros, M., & Johnson, H. P. (1986). Bookshelf tectonics: Rotated crustal blocks within the Sovanco Fracture Zone. *Geophysical Research Letters*, *13*(10), 995–998. https://doi.org/10.1029/GL013i010p00995

Dannowski, A., Morgan, J. P., Grevemeyer, I., & Ranero, C. R. (2018). Enhanced mantle upwelling/melting caused segment propagation, oceanic core complex die off, and the death of a transform fault: The Mid-Atlantic Ridge at 21.5°N. *Journal of Geophysical Research: Solid Earth*, *123*(2), 941–956. https://doi.org/10.1002/2017JB014273

Dauteuil, O. (1995). Fault pattern from seabeam processing: The western part of the Blanco Fracture Zone (NE Pacific). *Marine Geophysical Researches*, *17*(1), 17–35. https://doi.org/10.1007/BF01268049

DeMets, C., Gordon, R. G., & Argus, D. F. (2010). Geologically current plate motions. *Geophysical Journal International*, *181*(1), 1–80. https://doi.org/10.1111/j.1365-246X.2009.04491.x

Distortions, A. S. (1989). Rotations and crustal thinning at ridge–transform intersections. *Nature*, *340*(6235), 626–628. https://doi.org/10.1038/340626a0

Dziak, R., Chadwick, W., Fox, C., & Embley, R. (2003). Hydrothermal temperature changes at the southern Juan de Fuca Ridge associated with MW 6.2 Blanco Transform earthquake. *Geology*, *31*(2), 119–122. https://doi.org/10.1130/0091-7613(2003)031<0119:HTCATS>2.0.CO;2

Dziak, R., Fox, C., & Embley, R. (1991). Relationship between the seismicity and geologic structure of the Blanco Transform Fault Zone. *Marine Geophysical Researches*, *13*(3), 203–208. https://doi.org/10.1007/BF00369149

Dziak, R., Fox, C., Embley, R., Nábělek, J., Braunmiller, J., & Koski, R. (2000). Recent tectonics of the Blanco Ridge, eastern Blanco transform fault zone. *Marine Geophysical Researches*, *21*(5), 423–450. https://doi.org/10.1023/A:1026545910893

Ekström, G., Nettles, M., & Dziewoński, A. M. (2012). The global CMT project 2004–2010: Centroid-moment tensors for 13,017 earthquakes. *Physics of the Earth and Planetary Interiors*, *200–201*, 1–9. https://doi.org/10.1016/j.pepi.2012.04.002

Elvers, D., Srivastava, S., Potter, K., Morley, J., & Sdidel, D. (1973). Asymmetric spreading across the Juan de Fuca and Gorda rises as obtained from a detailed magnetic survey. *Earth and Planetary Science Letters*, *20*(2), 211–219. https://doi.org/10.1016/0012-821X(73)90160-X

Embley, R. W., & Wilson, D. S. (1992). Morphology of the Blanco Transform Fault Zone-NE Pacific: Implications for its Tectonic Evolution. *Marine Geophysical Researches*, *14*(1), 25–45. https://doi.org/10.1007/BF01674064

Fornari, D. J., Gallo, D. G., Edwards, M. H., Madsen, J. A., Perfit, M. R., & Shor, A. N. (1989). Structure and topography of the Siqueiros transform fault system: Evidence for the development of intra-transform spreading centers. *Marine Geophysical Researches*, *11*(4), 263–299. https://doi.org/10.1007/BF00282579

Furlong, K. P., Sheaffer, S. D., & Malservisi, R. (2001). Thermal-rheological controls on deformation within oceanic transforms. *Geological Society, London, Special Publications*, *186*(1), 65–83. https://doi.org/10.1144/GSL.SP.2001.186.01.05

Gallo, D. G., Fox, P. J., & Macdonald, K. C. (1986). A Sea Beam investigation of the Clipperton transform fault: The morphotectonic expression of a fast-slipping transform boundary. *Journal of Geophysical Research*, *91*(B3), 3455–3467. https://doi.org/10.1029/JB091iB03p03455

Géli, L., Piau, J., Dziak, R., Maury, V., Fitzenz, D., Coutellier, Q., et al. (2014). Seismic precursors linked to highly compressible fluids at oceanic transform faults. *Nature Geoscience*, *7*(10), 757–761. https://doi.org/10.1038/ngeo2244

Gerya, T. V. (2012). Origin and models of oceanic transform faults. *Tectonophysics*, *522–533*, 34–54. https://doi.org/10.1016/j.tecto.2011.07.006

GFZ & Gempa GmbH. (2008). *The SeisComP seismological software package*. GFZ Data Services. https://doi.org/10.5880/GFZ.2.4.2020.003

Gong, J., Fan, W., & Parnell-Turner, R. (2022). Microseismicity indicates atypical small-scale plate rotation at the Quebrada transform fault system, East Pacific Rise. *Geophysical Research Letters*, *49*(3), e2021GL097000. https://doi.org/10.1029/2021GL097000

Grevemeyer, I., Hayman, N. W., Lange, D., Peirce, C., Papenberg, C., Van Avendonk, H. J. A., et al. (2019). Constraining the maximum depth of brittle deformation at slow- and ultraslow-spreading ridges using microseismicity. *Geology*, *47*(11), 1069–1073. https://doi.org/10.1130/G46577.1

Grevemeyer, I., Reston, T. J., & Moeller, S. (2013). Microseismicity of the Mid-Atlantic Ridge at 7°S–8°15′S and at the Logatchev Massif oceanic core complex at 14°40′N–14°50′N. *Geochemistry, Geophysics, Geosystems*, *14*(9), 3532–3554. https://doi.org/10.1002/ggge.20197

Grevemeyer, I., Rüpke, L. H., Morgan, J. P., Iyer, K., & Devey, C. W. (2021). Extensional tectonics and two-stage crustal accretion at oceanic transform faults. *Nature*, *591*(7850), 402–407. https://doi.org/10.1038/s41586-021-03278-9

Hart, R., Hoefs, J., & Pyle, D. (1990). Multistage hydrothermal systems in the Blanco Fracture Zone. In G. R. McMurray (Ed.), *Gorda Ridge* (pp. 51–75). Springer. https://doi.org/10.1007/978-1-4612-3258-2_4

Husen, S., Kissling, E., Flueh, E., & Asch, G. (1999). Accurate hypocentre determination in the seismogenic zone of the subducting Nazca Plate in northern Chile using a combined on-/offshore network. *Geophysical Journal International*, *138*(3), 687–701. https://doi.org/10.1046/j.1365-246x.1999.00893.x

Hutton, L. K., & Boore, D. M. (1987). The ML scale in Southern California. *Bulletin of the Seismological Society of America*, *77*(6), 2074–2094. https://doi.org/10.1785/BSSA0770062074

Johnson, S. H., & Jones, P. R. (1978). Microearthquakes located on the Blanco Fracture Zone with sonobuoy arrays. *Journal of Geophysical Research*, *83*(B1), 255–261. https://doi.org/10.1029/JB083iB01p00255

Kahle, R., Tilmann, F., & Grevemeyer, I. (2016). Crustal structure and kinematics of the TAMMAR propagating rift system on the Mid-Atlantic Ridge from seismic refraction and satellite altimetry gravity. *Geophysical Journal International*, *206*(2), 1382–1397. https://doi.org/10.1093/gji/ggw219

Karson, J. A. (2017). The Iceland plate boundary zone: Propagating rifts, migrating transforms, and rift-parallel strike-slip faults. *Geochemistry, Geophysics, Geosystems*, *18*(11), 4043–4054. https://doi.org/10.1002/2017GC007045

Karsten, J. L., & Delaney, J. R. (1989). Hot spot-ridge crest convergence in the northeast Pacific. *Journal of Geophysical Research*, *94*(B1), 700–712. https://doi.org/10.1029/JB094iB01p00700

Kissling, E., Ellsworth, W. L., Eberhart-Phillips, D., & Kradolfer, U. (1994). Initial reference models in local earthquake tomography. *Journal of Geophysical Research*, *99*(B10), 19635–19646. https://doi.org/10.1029/93JB03138

Kuna, V. M. (2020). Investigation of slip and tectonics of the Blanco Transform Fault using high-resolution ocean bottom seismic data. Ph.D. thesis. Oregon State University.
Kuna, V. M., Nábělek, J. L., & Braunmiller, J. (2019). Mode of slip and crust–mantle interaction at oceanic transform faults. *Nature Geoscience*, *12*(2), 138–142. https://doi.org/10.1038/s41561-018-0287-1
Lange, D., Rietbrock, A., Haberland, C., Bataille, K., Dahm, T., Tilmann, F., & Flüh, E. R. (2007). Seismicity and geometry of the south Chilean subduction zone (41.5°S–43.5°S): Implications for controlling parameters. *Geophysical Research Letters*, *34*(6), L06311. https://doi.org/10.1029/2006GL029190
Lomax, A., Virieux, J., Volant, P., & Berge-Thierry, C. (2000). Probabilistic earthquake location in 3D and layered models. In C. H. Thurber, & N. Rabinowitz (Eds.), *Advances in seismic event location* (Vol. 18, pp. 101–134). Springer. https://doi.org/10.1007/978-94-015-9536-0_5
Lonsdale, P. (2005). Creation of the Cocos and Nazca plates by fission of the Farallon plate. *Tectonophysics*, *404*(3–4), 237–264. https://doi.org/10.1016/j.tecto.2005.05.011
Macdonald, K., Fox, P., Perram, L., Eisen, M., Haymon, R., Miller, S., et al. (1988). A new view of the mid-ocean ridge from the behavior of ridge-axis discontinuities. *Nature*, *335*(6187), 217–225. https://doi.org/10.1038/335217a0
Mann, P., Hempton, M. R., Bradley, D. C., & Burke, K. (1983). Development of Pull-Apart Basins. *The Journal of Geology*, *91*(5), 529–554. https://doi.org/10.1086/628803
Marjanović, M., Carbotte, S. M., Nedimović, M. R., & Canales, J. P. (2011). Gravity and seismic study of crustal structure along the Juan de Fuca Ridge axis and across pseudofaults on the ridge flanks. *Geochemistry, Geophysics, Geosystems*, *12*(5), Q05008. https://doi.org/10.1029/2010GC003439
Matthews, K. J., Müller, R. D., Wessel, P., & Whittaker, J. M. (2011). The tectonic fabric of the ocean basins. *Journal of Geophysical Research*, *116*(B12), B12109. https://doi.org/10.1029/2011JB008413
McKenzie, D. (1986). The geometry of propagating rifts. *Earth and Planetary Science Letters*, *77*(2), 176–186. https://doi.org/10.1016/0012-821X(86)90159-7
Menard, H. W. (1967). Extension of Northeastern-Pacific Fracture Zones. *Science*, *155*(3758), 72–74. https://doi.org/10.1126/science.155.3758.72
Morgan, W. J. (1968). Rises, trenches, great faults, and crustal blocks. *Journal of Geophysical Research*, *73*(6), 1959–1982. https://doi.org/10.1029/JB073i006p01959
Morgan, J. P., & Kleinrock, M. C. (1991). Transform zone migration: Implications of bookshelf faulting at oceanic and Icelandic propagating ridges. *Tectonics*, *10*(5), 920–935. https://doi.org/10.1029/90TC02481
Morgan, J. P., & Parmentier, E. M. (1984). Lithospheric stress near a ridge-transform intersection. *Geophysical Research Letters*, *11*(2), 113–116. https://doi.org/10.1029/GL011i002p00113
Nábělek, J., & Braunmiller, J. (2012). Plate Boundary Evolution and Physics at an Oceanic Transform Fault System [Dataset]. International Federation of Digital Seismograph Networks. https://doi.org/10.7914/SN/X9_2012
Nedimović, M. R., Bohnenstiehl, D. R., Carbotte, S. M., Canales, J. P., & Dziak, R. P. (2009). Faulting and hydration of the Juan de Fuca plate system. *Earth and Planetary Science Letters*, *284*(1–2), 94–102. https://doi.org/10.1016/j.epsl.2009.04.013
Ottemöller, L., & Havskov, J. (2003). Moment magnitude determination for local and regional earthquakes based on source spectra. *Bulletin of the Seismological Society of America*, *93*(1), 203–214. https://doi.org/10.1785/0120010220
Pickle, R. C., Forsyth, D. W., Harmon, N., Nagle, A. N., & Saal, A. (2009). Thermo-mechanical control of axial topography of intra-transform spreading centers. *Earth and Planetary Science Letters*, *284*(3–4), 343–351. https://doi.org/10.1016/j.epsl.2009.05.004
Pockalny, R. A., Fox, P. J., Fornari, D. J., Macdonald, K. C., & Perfit, M. R. (1997). Tectonic reconstruction of the Clipperton and Siqueiros Fracture Zones: Evidence and consequences of plate motion change for the last 3 Myr. *Journal of Geophysical Research*, *102*(B2), 3167–3181. https://doi.org/10.1029/96JB03391
Prigent, C., Warren, J. M., Kohli, A. H., & Teyssier, C. (2020). Fracture-mediated deep seawater flow and mantle hydration on oceanic transform faults. *Earth and Planetary Science Letters*, *532*, 115988. https://doi.org/10.1016/j.epsl.2019.115988
Reasenberg, P., & Oppenheimer, D. (1985). FPFIT, FPPLOT, and FPPAGE: Fortran computer programs for calculating and displaying earthquake fault-plane solutions. USGS Open File Report, 85-739. https://doi.org/10.3133/ofr85739
Ren, Y., Geersen, J., & Grevemeyer, I. (2022). Impact of spreading rate and age-offset on oceanic transform fault morphology. *Geophysical Research Letters*, *49*(2), e2021GL096170. https://doi.org/10.1029/2021GL096170
Roland, E., Behn, M. D., & Hirth, G. (2010). Thermal-mechanical behavior of oceanic transform faults: Implications for the spatial distribution of seismicity. *Geochemistry, Geophysics, Geosystems*, *11*(7), Q07001. https://doi.org/10.1029/2010GC003034
Ryan, W. B. F., Carbotte, S. M., Coplan, J. O., O'Hara, S., Melkonian, A., Arko, R., et al. (2009). Global multi-resolution topography synthesis. *Geochemistry, Geophysics, Geosystems*, *10*(3), Q03014. https://doi.org/10.1029/2008GC002332
Skolotnev, S., Sanfilippo, A., Peyve, A., Nestola, Y., Sokolov, S., Petracchini, L., et al. (2021). Seafloor spreading and tectonics at the Charlie Gibbs transform system (52-53°N, mid Atlantic ridge): Preliminary results from R/V AN Strakhov expedition S50. *Ofioliti*, *46*(1), 83–101. https://doi.org/10.4454/ofioliti.v46i1.539
van Wijk, J., Axen, G., & Abera, R. (2017). Initiation, evolution and extinction of pull-apart basins: Implications for opening of the Gulf of California. *Tectonophysics*, *719–720*, 37–50. https://doi.org/10.1016/j.tecto.2017.04.019
Williams, J., Hawthorne, J., Rost, S., & Wright, T. (2019). Stress drops on the Blanco oceanic transform fault from interstation phase coherence. *Bulletin of the Seismological Society of America*, *109*(3), 929–943. https://doi.org/10.1785/0120180319
Wilson, D. S. (1990). Kinematics of overlapping rift propagation with cyclic rift failure. *Earth and Planetary Science Letters*, *96*(3–4), 384–392. https://doi.org/10.1016/0012-821X(90)90014-O
Wilson, D. S. (1988). Tectonic history of the Juan de Fuca Ridge over the last 40 million years. *Journal of Geophysical Research*, *93*(B10), 11863–11876. https://doi.org/10.1029/JB093iB10p11863
Wilson, D. S. (1993). Confidence intervals for motion and deformation of the Juan de Fuca Plate. *Journal of Geophysical Research*, *98*(B9), 16053–16071. https://doi.org/10.1029/93JB01227
Wilson, D. S., Hey, R. N., & Nishimura, C. (1984). Propagation as a mechanism of reorientation of the Juan de Fuca Ridge. *Journal of Geophysical Research*, *89*(B11), 9215–9225. https://doi.org/10.1029/JB089iB11p09215
Wilson, J. T. (1965). A new class of faults and their bearing on continental drift. *Nature*, *207*(4995), 343–347. https://doi.org/10.1038/207343a0
Wolfson-Schwehr, M., & Boettcher, M. S. (2019). Global characteristics of oceanic transform fault structure and seismicity. In J. C. Duarte (Ed.), *Transform plate boundaries and fracture zones* (pp. 21–59). Elsevier. https://doi.org/10.1016/B978-0-12-812064-4.00002-5
Yu, Z., Singh, S. C., Gregory, E. P. M., Maia, M., Wang, Z., & Brunelli, D. (2021). Semi-brittle seismic deformation in high-temperature mantle mylonite shear zone along the Romanche transform fault. *Science Advances*, *7*(15), eabf3388. https://doi.org/10.1126/sciadv.abf3388

References From the Supporting Information

Álvarez-Gómez, J. A. (2019). FMC—Earthquake focal mechanisms data management, cluster and classification. *SoftwareX*, *9*, 299–307. https://doi.org/10.1016/j.softx.2019.03.008

Engdahl, E. R. (2006). Application of an improved algorithm to high precision relocation of ISC test events. *Physics of the Earth and Planetary Interiors*, *158*(1), 14–18. https://doi.org/10.1016/j.pepi.2006.03.007

Sandwell, D. T., Müller, R. D., Smith, W. H. F., Garcia, E., & Francis, R. (2014). New global marine gravity model from CryoSat-2 and Jason-1 reveals buried tectonic structure. *Science*, *346*(6205), 65–67. https://doi.org/10.1126/science.1258213